EE571 Final Project Report
State Estimation and Optimal Control of a 6-Mass Spring System

Yunus Emre Danabaş
(yunusdanabas@sabanciuniv.edu - 29359)

January 11, 2026

Contents

1 Introduction **3**
- 1.1 System description . . . 3
- 1.2 Objectives . . . 3

2 Part 0: Baseline Verification **4**
- 2.1 Objective . . . 4
- 2.2 System model . . . 4
- 2.3 Methodology: ZOH discretization . . . 4
- 2.4 Initial conditions . . . 5
- 2.5 Results . . . 5
- 2.6 Findings . . . 6

3 Part 1: Observability Analysis **7**
- 3.1 Objective . . . 7
- 3.2 Theory . . . 7
- 3.3 Methodology . . . 7
- 3.4 Results . . . 8
- 3.5 Eigenvalue analysis (modal interpretation) . . . 8
- 3.6 Findings . . . 8

4 Part 2: Observer Design **9**
- 4.1 Objective . . . 9
- 4.2 Sensor configuration . . . 9
- 4.3 Observer design . . . 9
- 4.4 Initial conditions and simulation setup . . . 10
- 4.5 Results . . . 10
- 4.6 Numerical notes . . . 12
- 4.7 Findings . . . 12

5 Part 3: LQR Controller Design **13**
- 5.1 Objective . . . 13
- 5.2 LQR design . . . 13
- 5.3 Closed-loop dynamics . . . 13
- 5.4 Results . . . 13
- 5.5 Findings . . . 16

6 Part 4: Reduced Input LQR Controller **17**
- 6.1 Objective . . . 17
- 6.2 Input matrix reduction . . . 17
- 6.3 LQR redesign . . . 17
- 6.4 Implementation . . . 17
- 6.5 Results . . . 17
- 6.6 Findings . . . 20

7 Part 5: Kalman Filter Design **21**
7.1 Objective . . . 21
7.2 Noise Model . . . 21
7.3 Sensor Configuration . . . 21
7.4 Kalman Filter Design . . . 21
7.5 Results . . . 22
7.6 Comparison with Part 2 Observer . . . 25
7.7 Findings . . . 25

8 Part 6: LQG Controller **25**
8.1 Objective . . . 25
8.2 LQG structure . . . 25
8.3 Closed-loop dynamics . . . 26
8.4 Cost function under measurement noise . . . 26
8.5 Results . . . 26
8.6 Figures . . . 27
8.7 Findings . . . 28

9 Part 7: Sensor Augmentation Analysis **29**
9.1 Objective . . . 29
9.2 Sensor configurations . . . 29
9.3 Design principles . . . 29
9.4 Results . . . 29
9.5 Performance improvements and diminishing returns . . . 32
9.6 Findings . . . 32

10 Conclusion **33**
10.1 Summary of key findings . . . 33
10.2 Key learnings . . . 33
10.3 Design recommendations . . . 33

1 Introduction

1.1 System description

This project studies a one-dimensional chain of six masses coupled by springs. The state vector is composed of six positions and six velocities:

$$x(t) = \begin{bmatrix} x_p(t) \\ v(t) \end{bmatrix}, \quad x_p(t) = \begin{bmatrix} x_1(t) \\ x_2(t) \\ x_3(t) \\ x_4(t) \\ x_5(t) \\ x_6(t) \end{bmatrix}, \quad v(t) = \begin{bmatrix} v_1(t) \\ v_2(t) \\ v_3(t) \\ v_4(t) \\ v_5(t) \\ v_6(t) \end{bmatrix}. \tag{1}$$

The system is actuated by three control inputs,

$$u(t) = \begin{bmatrix} u_1(t) & u_2(t) & u_3(t) \end{bmatrix}^\top \in \mathbb{R}^3, \tag{2}$$

and measured by an output vector whose dimension depends on the sensor configuration used in each part.

The continuous-time state-space model is

$$\dot{x}(t) = Ax(t) + Bu(t), \tag{3}$$
$$y(t) = Cx(t), \tag{4}$$

where $A \in \mathbb{R}^{12\times 12}$ encodes the coupled mass-spring dynamics, $B \in \mathbb{R}^{12\times 3}$ maps the three actuators into the state derivatives, and C selects the measured states.

The model is discretized with a zero-order hold (ZOH) using sampling time $T_s = 0.01\,\mathrm{s}$, yielding

$$x[k+1] = A_d x[k] + B_d u[k], \tag{5}$$
$$y[k] = C_d x[k]. \tag{6}$$

Throughout the report, $k \in \mathbb{Z}_{\geq 0}$ denotes the discrete-time index.

1.2 Objectives

The overall goal is to design and evaluate state estimation and optimal control strategies for the discretized 6-mass spring system. The project progresses from basic model verification to optimal estimation and control under stochastic disturbances, and finally to performance analysis under sensor augmentation.

A central regulation objective is expressed via the quadratic stage cost

$$\ell(x[k], u[k]) = u[k]^\top u[k] + y_1[k]^2 + y_6[k]^2, \tag{7}$$

and the finite-horizon cost

$$J = \sum_{k=0}^{N-1} \left(u[k]^\top u[k] + y_1[k]^2 + y_6[k]^2 \right), \tag{8}$$

which balances control effort against regulation of the end-mass displacements.

2 Part 0: Baseline Verification

2.1 Objective

Part 0 validates the baseline (open-loop) behavior of the 6-mass spring system after discretization. This verification step ensures three key aspects:

- The continuous-time state-space model is constructed correctly
- The continuous-to-discrete conversion is implemented properly
- The undriven response matches the expected physics of an undamped coupled oscillator chain

This baseline response serves as a reference for evaluating the performance of observers and controllers in subsequent parts.

2.2 System model

The continuous-time model is represented in state-space form as

$$\dot{x}(t) = Ax(t) + Bu(t), \tag{9}$$
$$y(t) = Cx(t), \tag{10}$$

where $x(t) \in \mathbb{R}^{12}$ contains the six displacements and six velocities, and $u(t) \in \mathbb{R}^3$ contains the three control inputs. The matrix dimensions are

$$A \in \mathbb{R}^{12\times12}, \quad B \in \mathbb{R}^{12\times3}, \quad C \in \mathbb{R}^{1\times12}.$$

In this baseline configuration, the output is a single measurement corresponding to the displacement of mass 1, so $y(t) = y_1(t) = x_1(t)$.

For digital simulation and later discrete-time design, the model is discretized with sampling time $T_s = 0.01\,\text{s}$ to obtain

$$x[k+1] = A_d x[k] + B_d u[k], \tag{11}$$
$$y[k] = C_d x[k], \tag{12}$$

with $A_d \in \mathbb{R}^{12\times12}$, $B_d \in \mathbb{R}^{12\times3}$, and $C_d \in \mathbb{R}^{1\times12}$.

2.3 Methodology: ZOH discretization

A zero-order hold (ZOH) assumption is used, meaning the input is held constant over each sampling interval $[kT_s, (k+1)T_s)$. The corresponding discrete-time matrices are

$$A_d = e^{AT_s}, \tag{13}$$
$$B_d = \int_0^{T_s} e^{A\tau}\, B\, d\tau, \tag{14}$$
$$C_d = C, \qquad D_d = 0. \tag{15}$$

The baseline simulation uses open-loop input $u[k] \equiv 0$ for $N = 1000$ steps, corresponding to a total simulated duration of $NT_s = 10\,\text{s}$.

2.4 Initial conditions

To excite the chain dynamics, the initial condition is chosen as a unit displacement on mass 6 with all other states at rest:

$$x[0] = \begin{bmatrix} 0 & 0 & 0 & 0 & 0 & 1 & 0 & 0 & 0 & 0 & 0 & 0 \end{bmatrix}^\top \tag{16}$$

This corresponds to stretching the last spring segment and then releasing the system with zero initial velocities.

2.5 Results

Figures 1 and 2 show the baseline time responses. The output $y[k] = x_1[k]$ remains oscillatory, and the displacements $x_1, \ldots, x_6$ illustrate how the initial deformation at mass 6 propagates through the coupled spring chain.

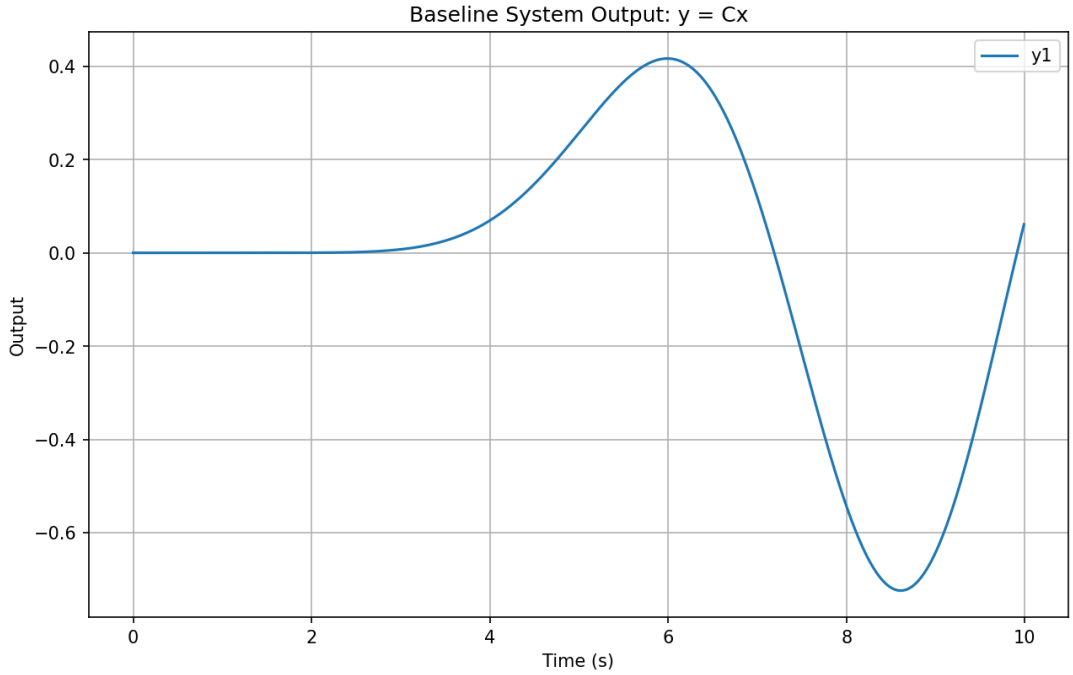

Figure 1: Baseline system output $y = Cx$ showing displacement of mass 1.

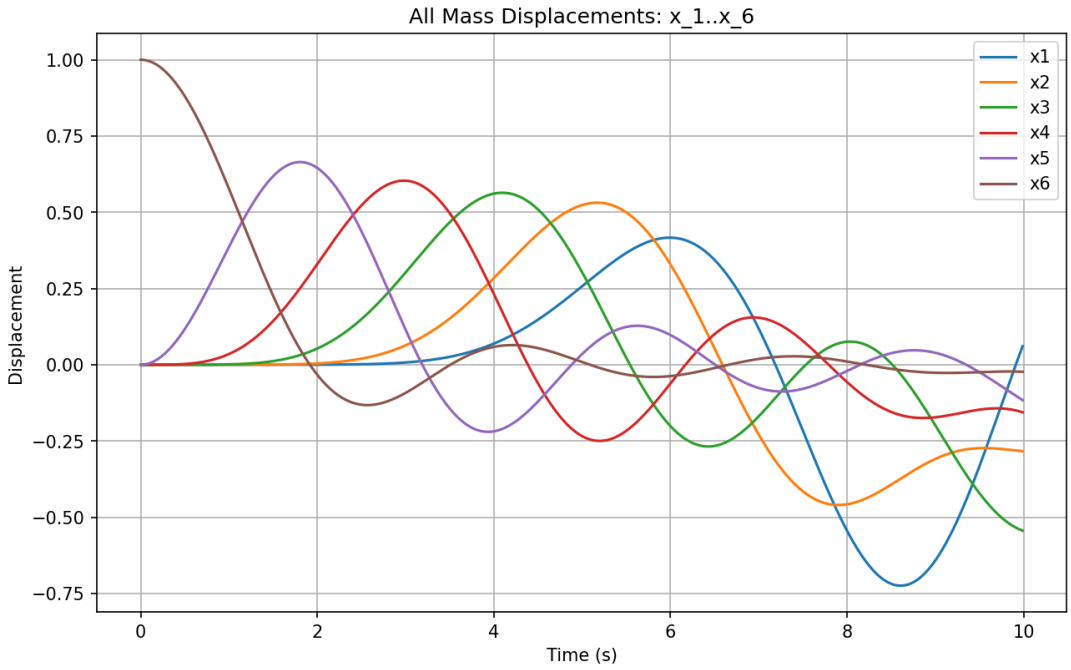

Figure 2: Open-loop displacements of all masses, x_1 through x_6, under the initial condition in (16).

2.6 Findings

- **Oscillatory behavior (undamped chain).** The responses are oscillatory because the model contains no dissipative elements. Energy alternates between potential energy in the springs and kinetic energy in the masses. Individual coordinates can show amplitude modulation because energy redistributes among coupled modes, even though the total energy is conserved.

- **Marginal stability.** The open-loop response does not converge to zero, which is consistent with an undamped mechanical system. In discrete time, this corresponds to eigenvalues of A_d lying on (or very near) the unit circle.

- **Energy propagation through the chain.** Starting from a displacement applied at mass 6, motion propagates through the spring couplings, exciting the upstream masses with phase shifts and different amplitudes, as seen in Fig. 2. This baseline propagation pattern is a key reference when evaluating the effect of estimation and control in later parts.

3 Part 1: Observability Analysis

3.1 Objective

Part 1 evaluates the *observability* of the discretized 6-mass spring system using only a single sensor that measures the displacement of mass 1 ($y[k] = x_1[k]$).

Observability determines whether the internal state $x[k]$ can be uniquely reconstructed from the measured output history $y[0], y[1], \ldots$ under known inputs $u[k]$. If some states are unobservable, then no observer—whether Luenberger or Kalman filter—can estimate them from the available measurements. This limitation directly affects achievable feedback performance when using estimated states.

3.2 Theory

Consider the discrete-time LTI model

$$x[k+1] = A_d x[k] + B_d u[k], \tag{17}$$

$$y[k] = C_d x[k], \tag{18}$$

with state dimension $n = 12$ and a single output ($p = 1$). The (discrete-time) observability matrix is

$$\mathcal{O} = \begin{bmatrix} C_d \\ C_d A_d \\ C_d A_d^2 \\ \vdots \\ C_d A_d^{n-1} \end{bmatrix} \in \mathbb{R}^{np \times n}. \tag{19}$$

The system is *fully observable* if and only if

$$\operatorname{rank}(\mathcal{O}) = n. \tag{20}$$

When $\operatorname{rank}(\mathcal{O}) = r < n$, the state space can be decomposed into observable and unobservable subspaces. The *Kalman decomposition* provides a similarity transform T such that, in transformed coordinates $\bar{x}[k] = T^{-1}x[k]$, the system matrices take a structured form:

$$\bar{A} = T^{-1} A_d T = \begin{bmatrix} A_{oo} & A_{ou} \\ 0 & A_{uu} \end{bmatrix}, \qquad \bar{C} = C_d T = \begin{bmatrix} C_o & 0 \end{bmatrix}, \tag{21}$$

where the first r transformed states are observable and the remaining $n - r$ states are unobservable (they do not affect the output).

3.3 Methodology

The following procedure is applied to the discretized model with $T_s = 0.01\,\text{s}$ and a single displacement sensor $y[k] = x_1[k]$:

- **SVD-based rank computation.** Construct $\mathcal{O}$ as in (19) and compute its numerical rank using singular value decomposition (SVD). A tolerance-based threshold is used to distinguish nonzero singular values from numerical noise.
- **Kalman decomposition.** Compute a well-conditioned similarity transform T that separates observable and unobservable subspaces, then extract the observable block A_{oo} and unobservable block A_{uu} in (21). The condition number $\kappa(T)$ is recorded to assess numerical reliability.

3.4 Results

The rank test shows the system is not fully observable with a single sensor measuring x_1. The Kalman decomposition confirms a clean separation into a 6-dimensional observable subspace and a 6-dimensional unobservable subspace.

Metric	Value
System dimension (n)	12
Observability rank	6
Observable states	6
Unobservable states	6
Transformation condition number	1.000010

Table 1: Observability analysis results.

3.5 Eigenvalue analysis (modal interpretation)

Because the mechanical chain is modeled as undamped, the continuous-time eigenvalues are (ideally) purely imaginary, $s = \pm j\omega$. Under ZOH discretization,

$$z = e^{sT_s} = e^{\pm j\omega T_s} = \cos(\omega T_s) \pm j \sin(\omega T_s), \tag{22}$$

which implies $|z| = 1$ for each undamped mode (up to small numerical deviations). Therefore, it is expected that eigenvalues of both A_{oo} and A_{uu} lie on or very near the unit circle.

Using the Kalman decomposition blocks, the distinct modal frequencies (in rad/s) are:

- **Observable mode frequencies:** 0.7653, 1.4139, 1.8475.
- **Unobservable mode frequencies:** 0.4451, 1.2469, 1.8017.

These frequencies correspond to different vibration modes. The fact that all eigenvalue magnitudes are near 1.0 reflects marginal stability of an undamped discrete-time oscillator, not a numerical error.

3.6 Findings

- **Not fully observable with a single sensor.** With only $y[k] = x_1[k]$, the observability rank is 6, so half of the 12-dimensional state is unobservable.
- **Mode-dependent observability.** Only modes that produce motion at mass 1 appear in the output and are therefore observable. Modes in which mass 1 does not participate (physically interpretable as antisymmetric patterns relative to the sensing location) are unobservable from x_1 alone.
- **Motivation for sensor augmentation.** Since unobservable states cannot be reconstructed by any observer, an additional sensor is required to capture the missing modes. This motivates adding a second displacement measurement in Part 2 to achieve full state observability.

4 Part 2: Observer Design

4.1 Objective

In Part 1, using only $y[k] = x_1[k]$ left a nontrivial unobservable subspace, which prevents full-state estimation. The objective of Part 2 is to design a discrete-time *Luenberger observer* using an augmented sensing configuration (measuring x_1 and x_6) so that all 12 states can be estimated from measured outputs and the known input.

4.2 Sensor configuration

Two displacement sensors are used:

$$y[k] = \begin{bmatrix} y_1[k] \\ y_6[k] \end{bmatrix} = \begin{bmatrix} x_1[k] \\ x_6[k] \end{bmatrix}, \qquad C = \begin{bmatrix} 1 & 0 & 0 & 0 & 0 & 0 & 0 & 0 & 0 & 0 & 0 & 0 \\ 0 & 0 & 0 & 0 & 0 & 1 & 0 & 0 & 0 & 0 & 0 & 0 \end{bmatrix} \in \mathbb{R}^{2\times 12}.$$

This configuration provides information from both ends of the chain, which is sufficient in practice to reconstruct the internal state evolution via the model dynamics.

4.3 Observer design

The discrete-time plant model is

$$x[k+1] = A_d x[k] + B_d u[k], \tag{23}$$
$$y[k] = Cx[k], \tag{24}$$

where $x[k] \in \mathbb{R}^{12}$, $u[k] \in \mathbb{R}^3$, and $y[k] \in \mathbb{R}^2$.

A Luenberger observer is chosen as

$$\hat{x}[k+1] = A_d \hat{x}[k] + B_d u[k] + L\big(y[k] - \hat{y}[k]\big), \tag{25}$$
$$\hat{y}[k] = C\hat{x}[k], \tag{26}$$

where $L \in \mathbb{R}^{12\times 2}$ is the observer gain. Defining the estimation error $e[k] = x[k] - \hat{x}[k]$, the error dynamics become

$$e[k+1] = (A_d - LC)\, e[k]. \tag{27}$$

Therefore, the observer is asymptotically stable if all eigenvalues of $(A_d - LC)$ lie strictly inside the unit circle.

Pole placement via the dual system. Observer pole placement for (A_d, C) is dual to state-feedback pole placement for $(A_d^\top, C^\top)$. A set of $n = 12$ distinct real poles is selected evenly in the range [0.4, 0.8], then placed for the dual system using a numerical pole placement routine. The resulting dual gain is transposed to obtain L. The achieved stability is summarized by the spectral radius

$$\rho(A_d - LC) = \max_i |\lambda_i(A_d - LC)|, \tag{28}$$

which is required to satisfy $\rho(A_d - LC) < 1$ for convergence.

4.4 Initial conditions and simulation setup

The plant and observer are initialized with mismatched initial conditions to test convergence:

$$x[0] = \begin{bmatrix} 0 & 0 & 0 & 1 & 1 & 1 & 0 & 0 & 0 & 0 & 0 & 0 \end{bmatrix}^\top, \tag{29}$$

$$\hat{x}[0] = \begin{bmatrix} 0 & 0 & 0 & 0 & 0 & 1 & 0 & 0 & 0 & 0 & 0 & 0 \end{bmatrix}^\top. \tag{30}$$

The simulation uses $T_s = 0.01\,\mathrm{s}$ and $N = 1000$ steps (10 seconds) with open-loop input $u[k] \equiv 0$.

4.5 Results

The designed observer gain has shape $L \in \mathbb{R}^{12\times 2}$, and the observer error dynamics are stable with spectral radius 0.8. RMS estimation errors are reported for the displacement states x_1 through x_6 over the full simulation window.

Metric	Value
Observer gain shape	(12, 2)
Spectral radius $\rho(A_d - LC)$	0.800000

Table 2: Observer design summary.

State	RMS error	Note
x_1 (measured)	2.4×10^{-7}	Near numerical precision
x_6 (measured)	5.1×10^{-6}	Near numerical precision
x_2	2.6×10^{-3}	Small
x_5	7.6×10^{-2}	Moderate
x_3	2.2	Larger (interior)
x_4	50.8	Largest (interior)

Table 3: RMS estimation errors for displacement states, grouped by magnitude.

Figures 3–5 visualize tracking of measured outputs and the displacement estimation errors.

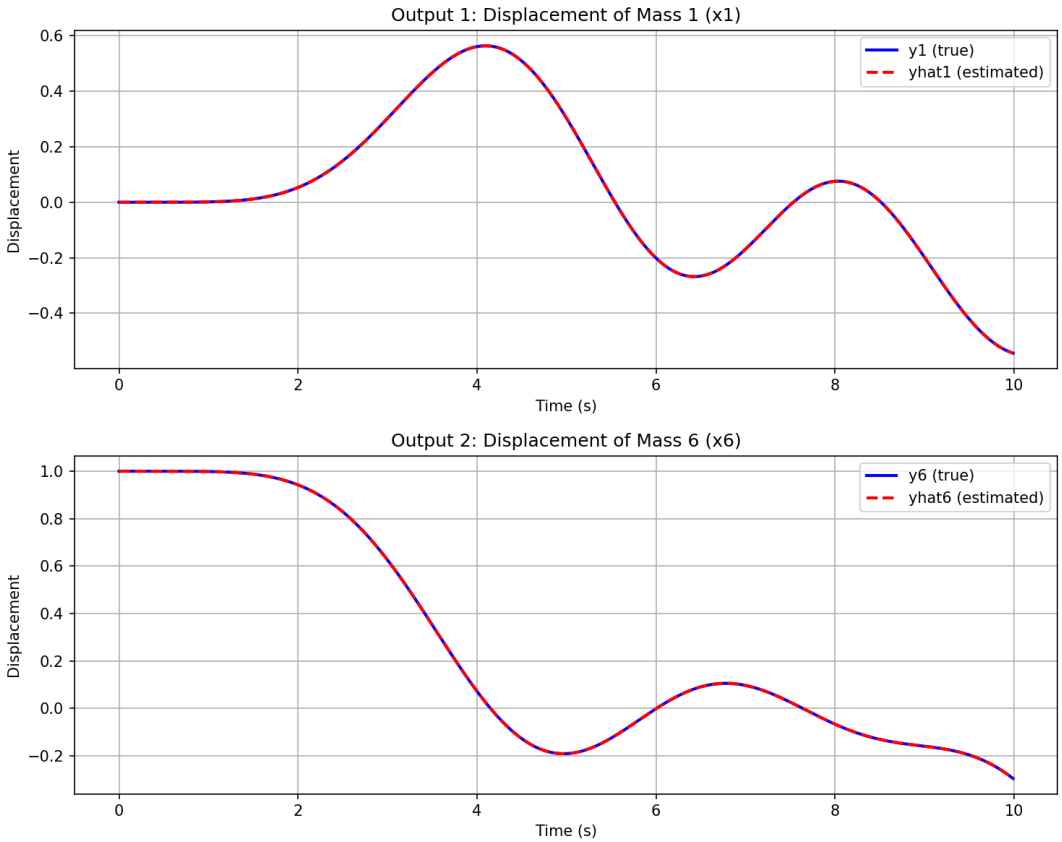

Figure 3: Measured outputs (x_1, x_6) and corresponding observer estimates. The estimated outputs closely match the measured signals.

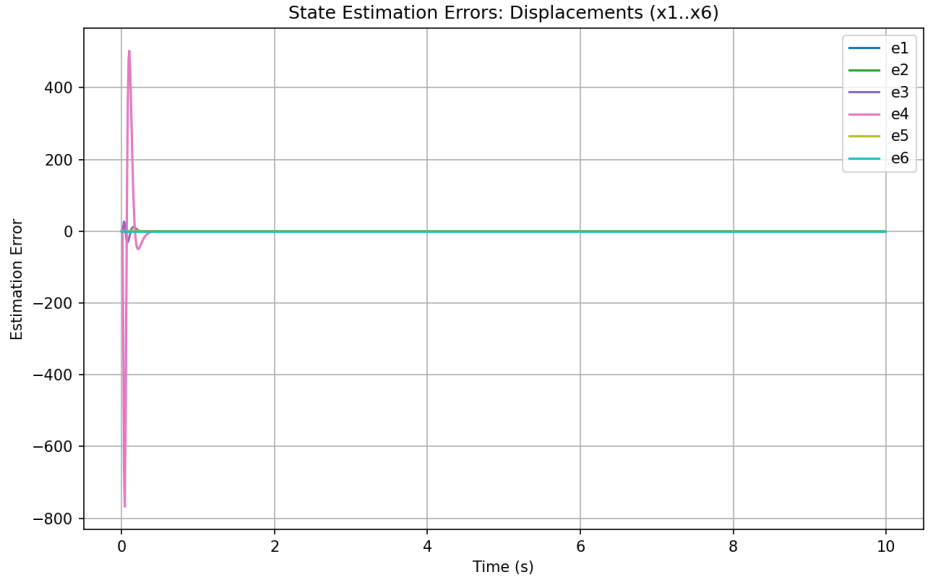

Figure 4: Estimation errors $e_i[k] = x_i[k] - \hat{x}_i[k]$ for displacement states (x_1 to x_6) over 10 seconds.

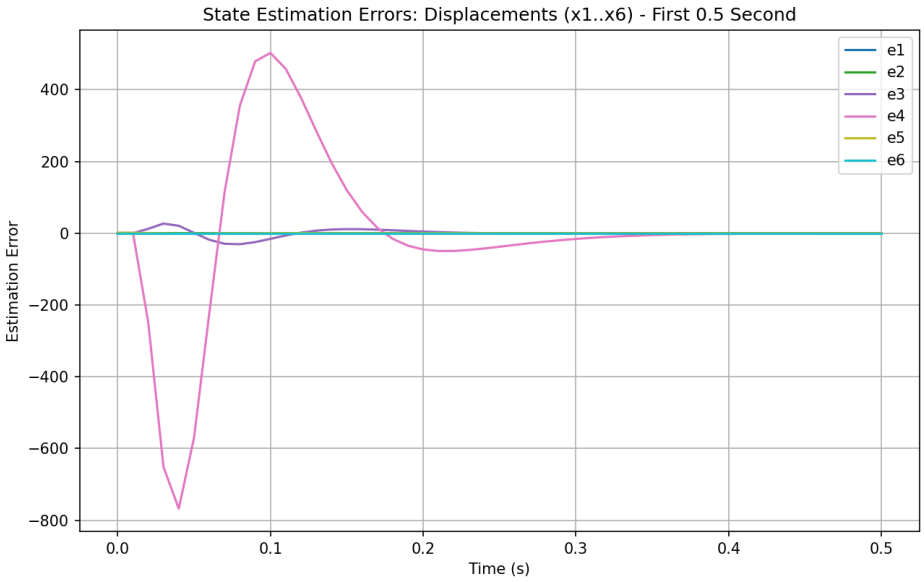

Figure 5: Zoomed view of the first 0.5 seconds of displacement estimation errors, highlighting the initial transient due to $x[0] \neq \hat{x}[0]$.

4.6 Numerical notes

The pole placement routine may emit a convergence warning due to numerical difficulty in 12-dimensional placement; however, stability is confirmed by verifying $\rho(A_d - LC) = 0.8 < 1$. A separate Qt platform warning in some Linux environments does not affect results.

4.7 Findings

- **Observer stability.** The designed observer is stable with $\rho(A_d - LC) = 0.8$, so estimation errors contract over time.
- **Measured states are estimated with very small error.** Since x_1 and x_6 are directly measured, their RMS errors are near numerical precision (on the order of 10^{-7} to 10^{-6}).
- **Unmeasured states show larger transient and RMS error.** Intermediate displacements, especially x_3 and x_4, exhibit larger errors due to the initial mismatch and the need to infer internal motion from boundary measurements. The errors remain bounded and decay after the initial transient, consistent with stable error dynamics.
- **Full-state estimation enabled by two sensors.** With the augmented measurements (x_1, x_6), the observer successfully reconstructs the full 12-state trajectory well enough to support estimated-state feedback in later parts.

5 Part 3: LQR Controller Design

5.1 Objective

The objective of Part 3 is to design a discrete-time Linear Quadratic Regulator (LQR) for the discretized 6-mass spring system and apply it using the estimated state $\hat{x}[k]$ obtained from the Part 2 Luenberger observer. The controller is designed to regulate the boundary displacements x_1 and x_6 toward zero while limiting control effort.

5.2 LQR design

The cost function from (8) is written in standard LQR form with weights

$$Q = C_y^\top C_y, \qquad R = I_3, \tag{31}$$

penalizing only x_1 and x_6 in the state cost. The discrete-time algebraic Riccati equation (DARE) yields the optimal gain

$$K = \left(R + B_d^\top P B_d\right)^{-1} B_d^\top P A_d \in \mathbb{R}^{3\times 12}, \tag{32}$$

where P is the stabilizing solution. The closed-loop matrix $A_{\text{cl}} = A_d - B_d K$ must satisfy $\rho(A_{\text{cl}}) < 1$ for stability.

Since the full state is not measured, the control law uses the observer estimate:

$$u[k] = -K\hat{x}[k]. \tag{33}$$

By the separation principle, K and L can be designed independently; the closed loop is stable when both $(A_d - B_d K)$ and $(A_d - L C_y)$ are stable.

5.3 Closed-loop dynamics

The combined plant, observer, and control law used in simulation are

$$x[k+1] = A_d x[k] + B_d u[k], \tag{34}$$

$$\hat{x}[k+1] = A_d \hat{x}[k] + B_d u[k] + L\big(y[k] - C_y \hat{x}[k]\big), \tag{35}$$

$$u[k] = -K\hat{x}[k], \tag{36}$$

with $y[k] = C_y x[k]$ and $\hat{y}[k] = C_y \hat{x}[k]$.

5.4 Results

Table 4 summarizes the key numerical results for the designed controller and the resulting closed-loop simulation.

Metric	Value
LQR gain K shape	(3, 12)
Closed-loop spectral radius $\rho(A_d - B_d K)$	0.999463
Total cost J	9.057478×10^7
Maximum input magnitude $\max_{i,k} \lvert u_i[k] \rvert$	3.597390×10^3
Observer spectral radius $\rho(A_d - L C_y)$	0.800000

Table 4: Part 3 LQR with observer. Summary of controller and closed-loop performance metrics.

Output regulation. Figure 6 shows the regulated outputs $y_1 = x_1$ and $y_6 = x_6$ under the observer-based LQR control law in (33).

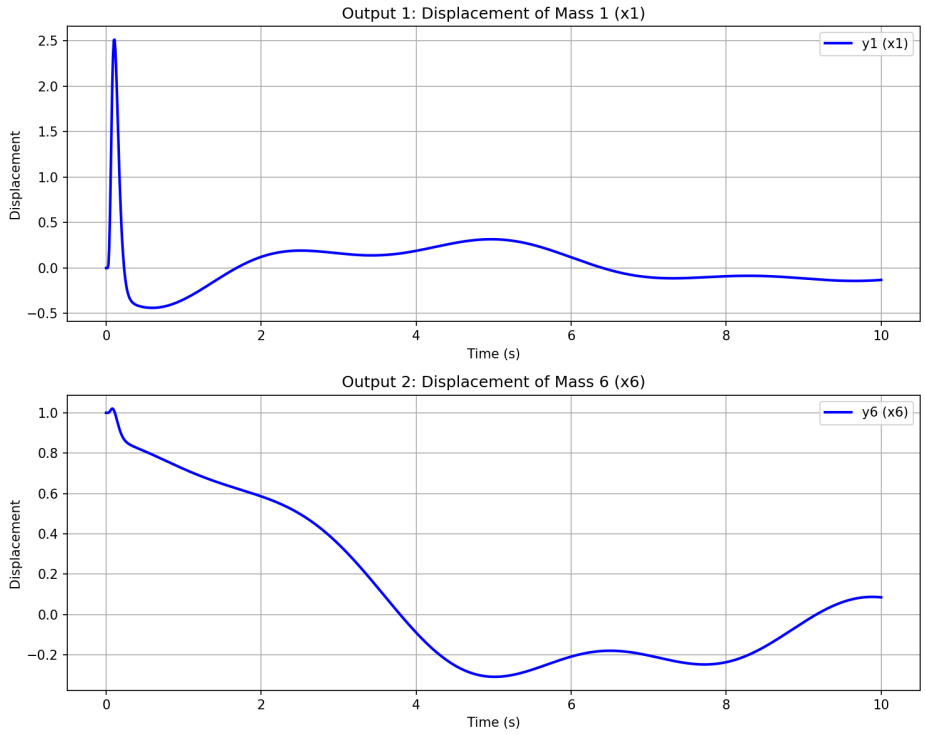

Figure 6: Closed-loop outputs under observer-based LQR. Top: $y_1 = x_1$. Bottom: $y_6 = x_6$.

Control inputs. Figure 7 shows the three control inputs. The inputs exhibit a large initial transient and then decay toward zero as the outputs are regulated.

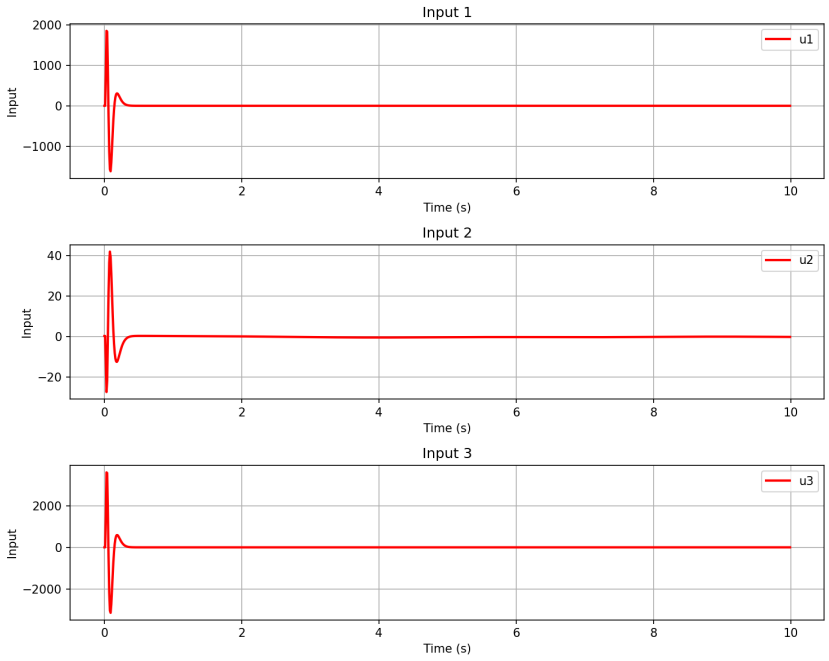

Figure 7: Closed-loop control inputs u_1, u_2, u_3 generated by $u[k] = -K\hat{x}[k]$.

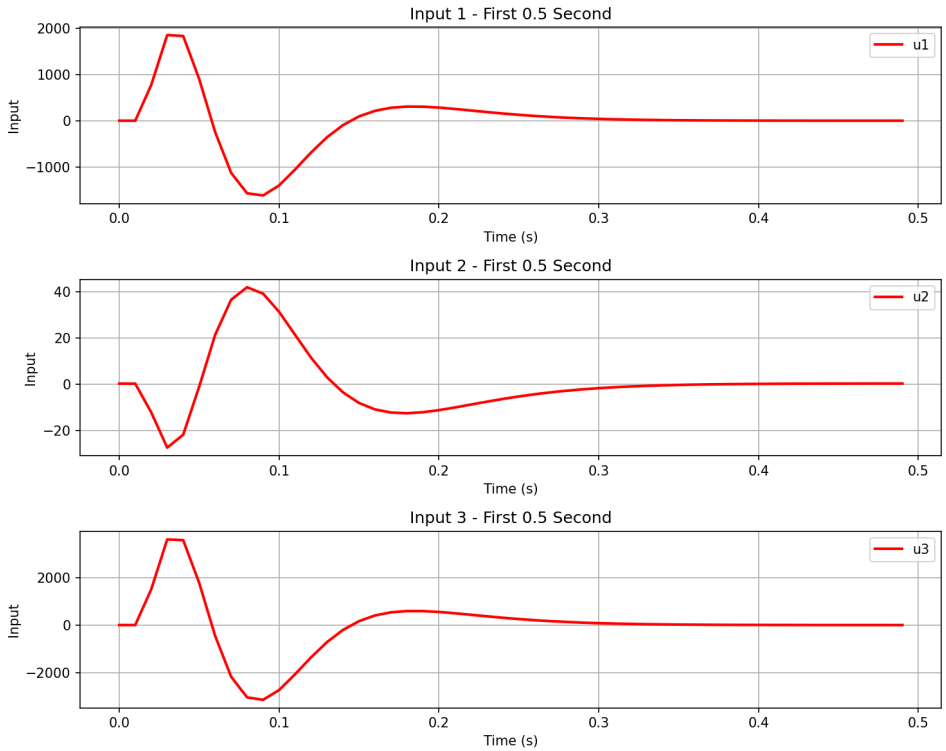

Figure 8: Zoomed view (first 0.5 s) of the closed-loop control inputs u_1, u_2, u_3, highlighting the initial transient.

Estimation error norm. To confirm that estimated-state feedback is well-justified, Fig. 9 plots the norm of the estimation error $\|x[k] - \hat{x}[k]\|$. Convergence of this error indicates that the observer transient decays and the controller effectively approaches true-state feedback behavior.

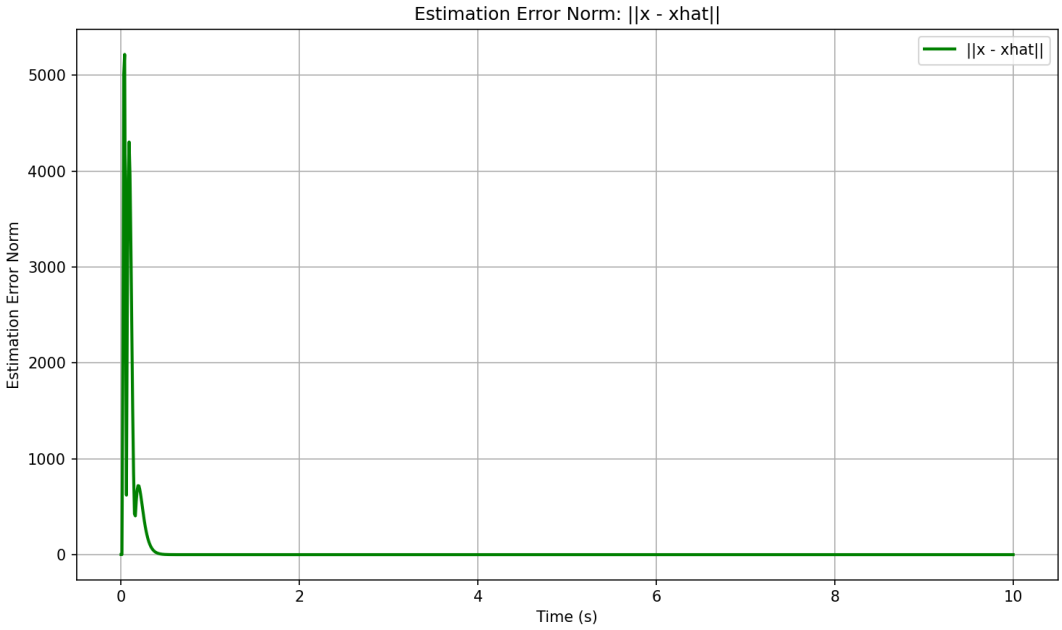

Figure 9: Estimation error norm $\|x - \hat{x}\|$ over time under observer-based LQR.

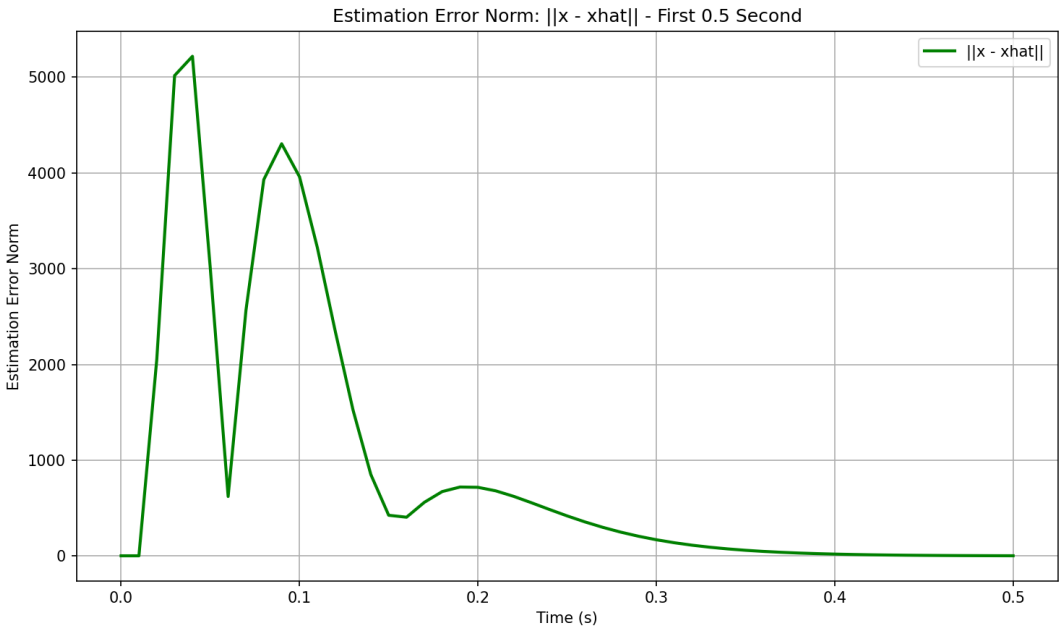

Figure 10: Zoomed view (first 0.5 s) of the estimation error norm $\|x - \hat{x}\|$, highlighting the observer transient.

5.5 Findings

- **Closed-loop stability.** The LQR design yields $\rho(A_d - B_d K) = 0.999463 < 1$, so the nominal closed-loop system is stable. The value is so close to 1.0, indicating slow convergence in the dominant closed-loop modes.

- **Output regulation.** Both $y_1 = x_1$ and $y_6 = x_6$ are driven toward zero, demonstrating that the chosen $Q = C_y^\top C_y$ correctly emphasizes boundary displacement regulation.

- **Estimated-state feedback works.** The observer remains stable with spectral radius 0.8, and the estimation error norm decays after the initial mismatch. This validates the separation principle in implementation, since the controller uses $u[k] = -K\hat{x}[k]$ rather than $-Kx[k]$.

- **Control effort.** The maximum input magnitude is 3.597×10^3, and the total cost is $J = 9.057 \times 10^7$ for the simulated horizon. These values reflect the trade-off between aggressive initial regulation and input energy penalization under $R = I_3$.

6 Part 4: Reduced Input LQR Controller

6.1 Objective

Part 4 evaluates the effect of reduced actuator authority by redesigning the LQR controller using only two inputs (u_1, u_2) instead of three (u_1, u_2, u_3). The goal is to quantify how removing one actuator impacts closed-loop stability, regulation performance of (x_1, x_6), and required control effort.

6.2 Input matrix reduction

The discrete-time plant from Part 3 is

$$x[k+1] = A_d x[k] + B_d u[k], \qquad y[k] = C_y x[k], \tag{37}$$

where $x \in \mathbb{R}^{12}$ and $u \in \mathbb{R}^3$. In this part, the third input u_3 is removed by selecting only the first two columns of B_d:

$$B_{d,\text{red}} = B_d(:, [1, 2]) \in \mathbb{R}^{12\times 2}, \qquad u_{\text{red}}[k] = \begin{bmatrix} u_1[k] \\ u_2[k] \end{bmatrix} \in \mathbb{R}^2. \tag{38}$$

The reduced-input plant becomes

$$x[k+1] = A_d x[k] + B_{d,\text{red}}\, u_{\text{red}}[k]. \tag{39}$$

6.3 LQR redesign

The DARE and gain computation follow Section 5 with $B_{d,\text{red}}$ replacing B_d and $R_{\text{red}} = I_2$. The state weight $Q = C_y^\top C_y$ is unchanged. The resulting gain is $K_{\text{red}} \in \mathbb{R}^{2\times 12}$, and the closed-loop matrix is $A_{\text{cl,red}} = A_d - B_{d,\text{red}} K_{\text{red}}$. Note that K_{red} must be recomputed via DARE; it cannot be obtained by simply deleting the third row of the Part 3 gain.

6.4 Implementation

As in Part 3, the control law uses the observer estimate: $u_{\text{red}}[k] = -K_{\text{red}}\hat{x}[k]$. Both plant and observer use $B_{d,\text{red}}$ for consistency.

6.5 Results

The reduced-input controller remains stable but exhibits degraded performance relative to the 3-input design. Table 5 compares the main metrics of Part 3 and Part 4.

Metric	Part 3 (3 inputs)	Part 4 (2 inputs)
LQR gain shape	(3, 12)	(2, 12)
Spectral radius	0.999463	0.999518
Total cost J	9.057×10^7	1.348×10^8
Max $\lvert u \rvert$	3.597×10^3	4.951×10^3
Cost increase	–	48.84%

Table 5: Comparison of full-input vs reduced-input LQR (observer-based implementation in both cases).

Outputs. Figure 11 shows $y_1 = x_1$ and $y_6 = x_6$ under reduced-input control.

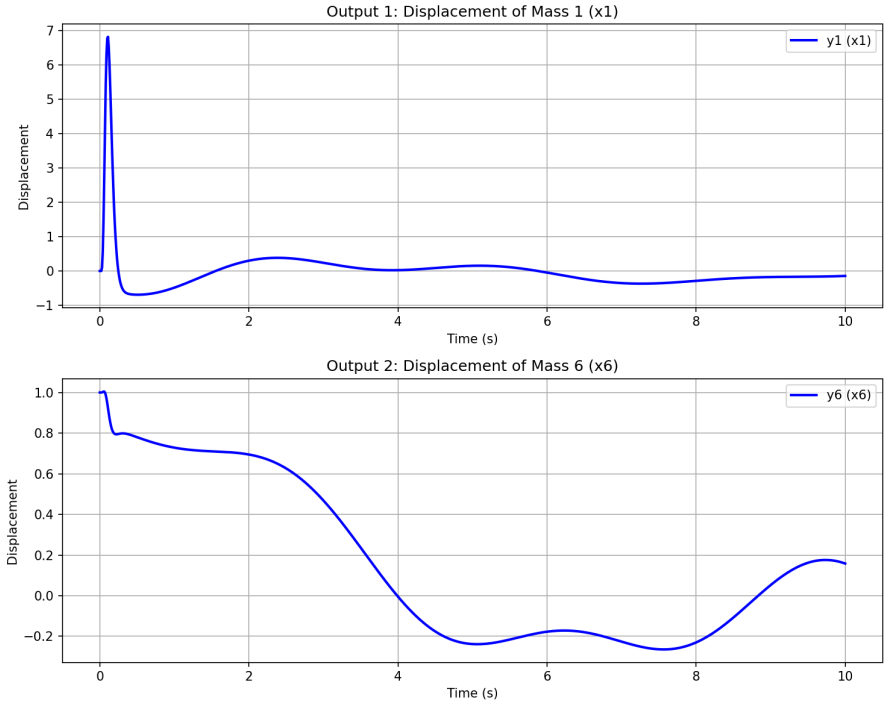

Figure 11: Closed-loop outputs under reduced-input observer-based LQR. Top: $y_1 = x_1$. Bottom: $y_6 = x_6$.

Control inputs. Figure 12 shows the two applied inputs over the full simulation horizon. Figure 13 provides a zoomed view of the first 0.5 s to highlight the initial transient.

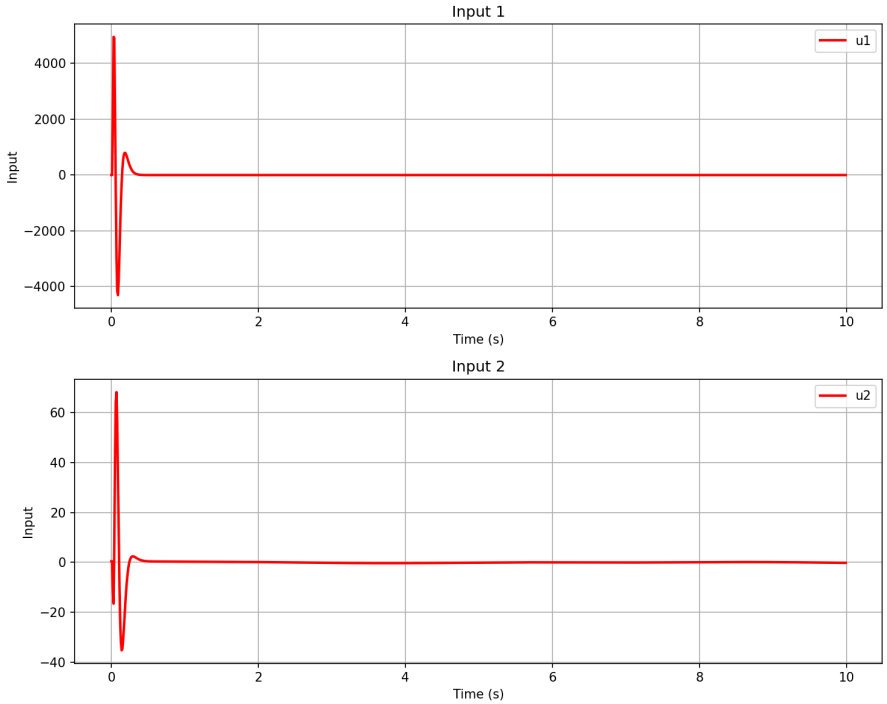

Figure 12: Reduced-input control signals u_1 and u_2 generated by $u_{\text{red}}[k] = -K_{\text{red}}\hat{x}[k]$.

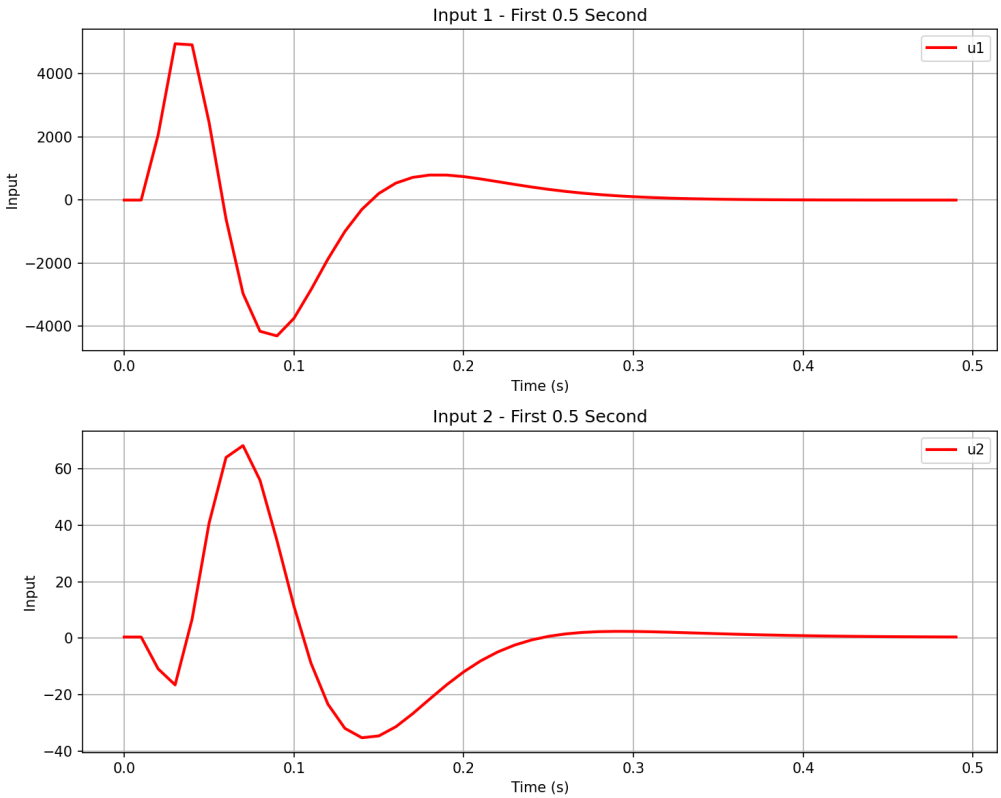

Figure 13: Zoomed view (first 0.5 s) of u_1 and u_2, highlighting the initial transient required to compensate for the removed actuator.

Estimation error norm. Figure 14 plots $\|x[k] - \hat{x}[k]\|$ over the full horizon. Figure 15 shows the first 0.5 s.

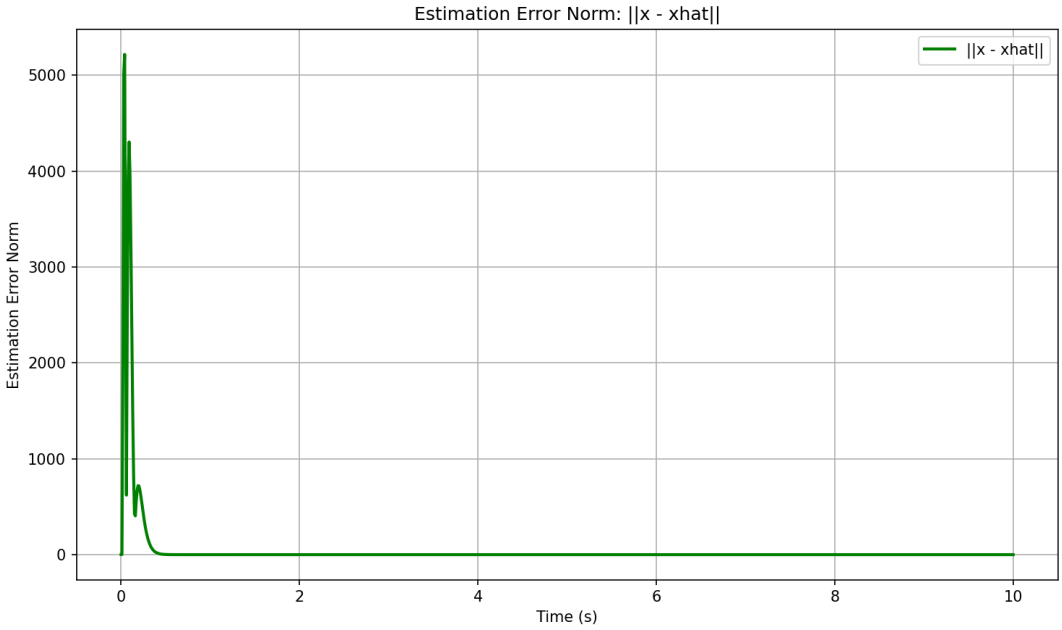

Figure 14: Estimation error norm $\|x - \hat{x}\|$ under reduced-input observer-based LQR.

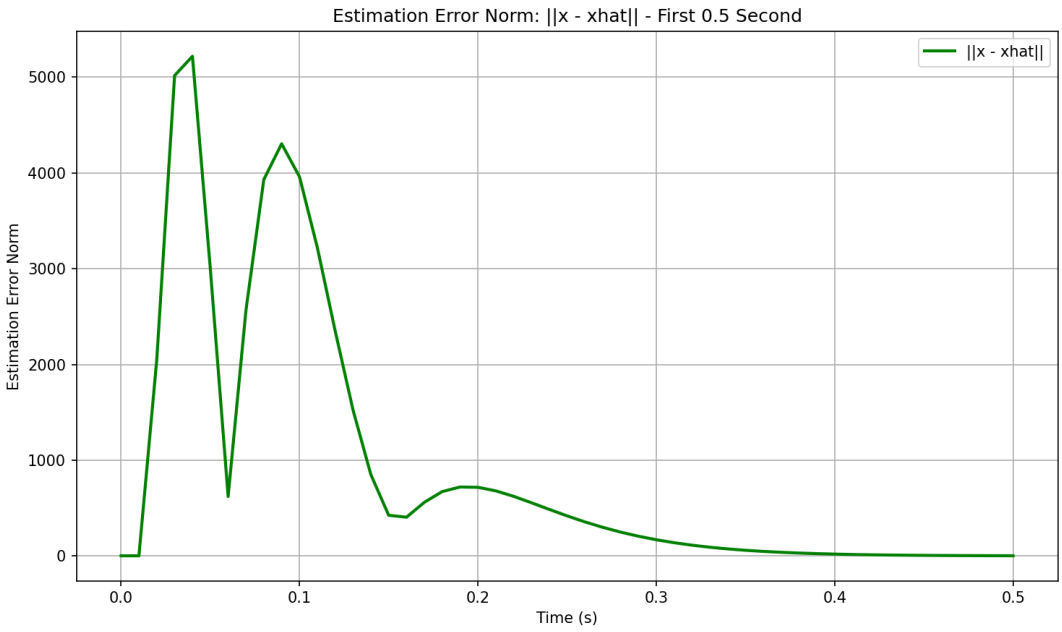

Figure 15: Zoomed view (first 0.5 s) of the estimation error norm $\|x - \hat{x}\|$.

6.6 Findings

- **Stability is preserved.** The reduced-input closed-loop spectral radius is $\rho(A_{\text{cl,red}}) = 0.999518 < 1$, so the system remains stable, with a dominant mode very close to the unit circle and therefore slow convergence.
- **Performance degrades with fewer actuators.** Removing u_3 increases the total cost by 48.84% (from 9.057×10^7 to 1.348×10^8), quantifying the loss of control authority.
- **Remaining actuators work harder.** The maximum input magnitude increases from 3.597×10^3 to 4.951×10^3, indicating higher effort in u_1 and u_2 to achieve comparable regulation.
- **Observer-based control remains valid.** The observer dynamics are unchanged in structure, and the estimation error norm decays after the initial transient, supporting the separation principle in the reduced-input setting.

7 Part 5: Kalman Filter Design

7.1 Objective

Parts 0–4 used deterministic models with a Luenberger observer designed via pole placement. In Part 5, the model is extended to a *stochastic* setting by introducing process noise (actuator disturbances) and measurement noise (sensor noise). The objective is to design a *steady-state discrete-time Kalman filter* that optimally estimates all 12 states from two noisy displacement measurements (mass 1 and mass 6).

The key difference from Part 2 is the design approach: the Luenberger observer uses pole placement to enforce a chosen convergence rate, while the Kalman filter uses known noise statistics to compute a gain that minimizes the steady-state estimation error covariance. Under standard linear Gaussian assumptions, the Kalman filter yields the minimum-variance linear estimate, making it the best linear unbiased estimator (BLUE).

7.2 Noise Model

The discrete-time plant (obtained via ZOH with $T_s = 0.01\,\mathrm{s}$) is modeled with additive actuator noise:

$$x[k+1] = A_d x[k] + B_d u[k] + B_d w[k], \tag{40}$$
$$y_{\mathrm{meas}}[k] = Cx[k] + v[k], \tag{41}$$

where $w[k]$ and $v[k]$ are zero-mean white noise sequences with covariances

$$\mathbb{E}\{w[k]w[k]^\top\} = Q_w, \qquad Q_w = 0.05\, I_3, \tag{42}$$
$$\mathbb{E}\{v[k]v[k]^\top\} = R_v, \qquad R_v = 0.1\, I_2. \tag{43}$$

Because the process noise enters through the input channels, the equivalent state-space process noise covariance is

$$Q_x = B_d Q_w B_d^\top \in \mathbb{R}^{12\times 12}. \tag{44}$$

7.3 Sensor Configuration

Two displacement sensors are used, measuring x_1 and x_6. The measurement matrix is

$$C = \begin{bmatrix} 1 & 0 & 0 & 0 & 0 & 0 & 0 & 0 & 0 & 0 & 0 & 0 \\ 0 & 0 & 0 & 0 & 0 & 1 & 0 & 0 & 0 & 0 & 0 & 0 \end{bmatrix} \in \mathbb{R}^{2\times 12}. \tag{45}$$

7.4 Kalman Filter Design

The discrete-time Kalman filter is the minimum-variance linear estimator for linear systems with (approximately) Gaussian noise. In steady-state form, the estimator uses a constant gain L_k and updates as

$$\hat{y}[k] = C\hat{x}[k], \tag{46}$$
$$\hat{x}[k+1] = A_d\hat{x}[k] + B_d u[k] + L_k\big(y_{\mathrm{meas}}[k] - \hat{y}[k]\big). \tag{47}$$

The term $y_{\mathrm{meas}}[k] - \hat{y}[k]$ is the *innovation* (measurement residual) used to correct the model prediction.

The steady-state error covariance P is obtained by solving the estimator DARE (the dual Riccati equation):

$$P = A_d P A_d^\top + Q_x \; - \; A_d P C^\top \big(C P C^\top + R_v\big)^{-1} C P A_d^\top, \tag{48}$$

which in implementation is computed via

$$P = \texttt{solve\_dare}\big(A_d^\top,\, C^\top,\, Q_x,\, R_v\big)\,. \tag{49}$$

The corresponding steady-state Kalman gain is

$$L_k = P C^\top \left(C P C^\top + R_v\right)^{-1} \in \mathbb{R}^{12\times 2}. \tag{50}$$

The associated estimation error dynamics are

$$e[k+1] = (A_d - L_k C)\, e[k] + B_d w[k] - L_k v[k], \tag{51}$$

and discrete-time estimator stability requires $\rho(A_d - L_k C) < 1$, where $\rho(\cdot)$ is the spectral radius.

7.5 Results

The filter was evaluated over $N = 1000$ steps (10 seconds) with the noise covariances in (40)–(44). The initial conditions match Part 2 (Section 4): $x[0] = [0,0,0,1,1,1,0,0,0,0,0,0]^\top$ (actual) and $\hat{x}[0] = [0,0,0,0,0,1,0,0,0,0,0,0]^\top$ (estimator), testing convergence under noise. To isolate estimator behavior, the simulation used zero control input ($u[k] = 0$), so the state evolution is driven only by process noise and the estimator correction.

Key numerical results are:

- Kalman gain shape: $L_k \in \mathbb{R}^{12\times 2}$
- Estimator spectral radius: $\rho(A_d - L_k C) = 0.999547$
- RMS estimation error (full window): 0.9607
- RMS estimation error (steady-state portion): 0.5313

The steady-state RMS error is reduced by

$$\frac{0.9607 - 0.5313}{0.9607} \approx 0.447, \tag{52}$$

which is approximately a 45% improvement after the initial transient.

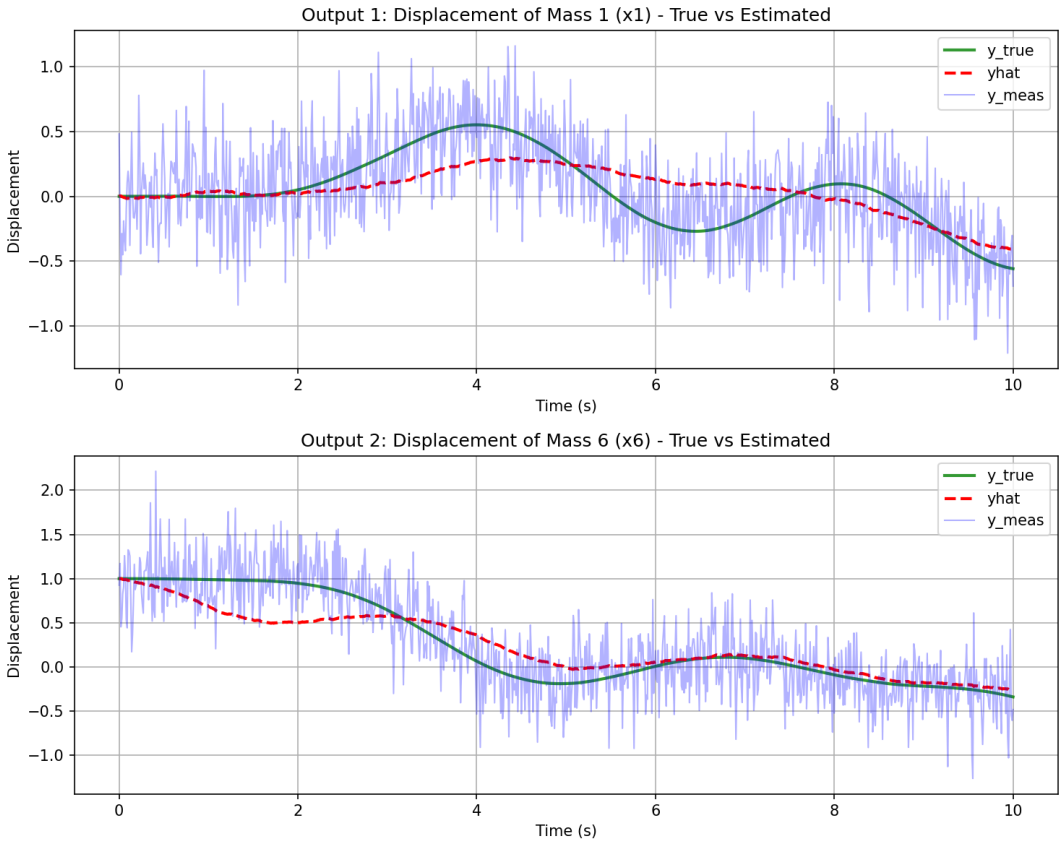

Figure 16: Noisy measurements and Kalman filter estimates for the measured outputs (x_1 and x_6). The estimate $\hat{y}$ tracks the true output while attenuating measurement noise in y_{meas}.

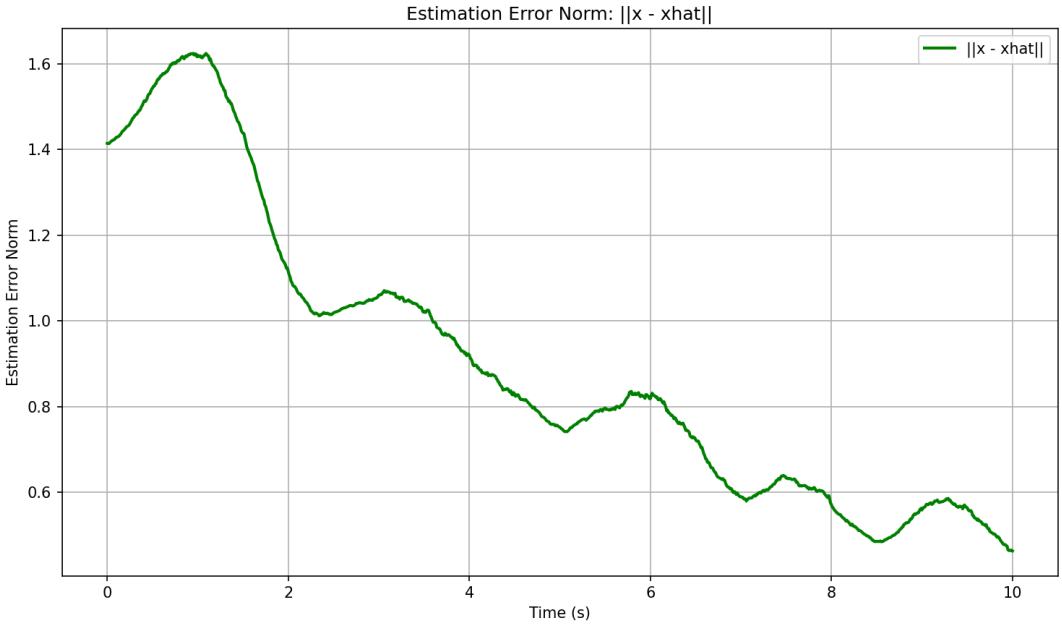

Figure 17: Estimation error norm $\|x - \hat{x}\|$ under process and measurement noise. The error decreases from its initial transient and then fluctuates around a lower steady-state level.

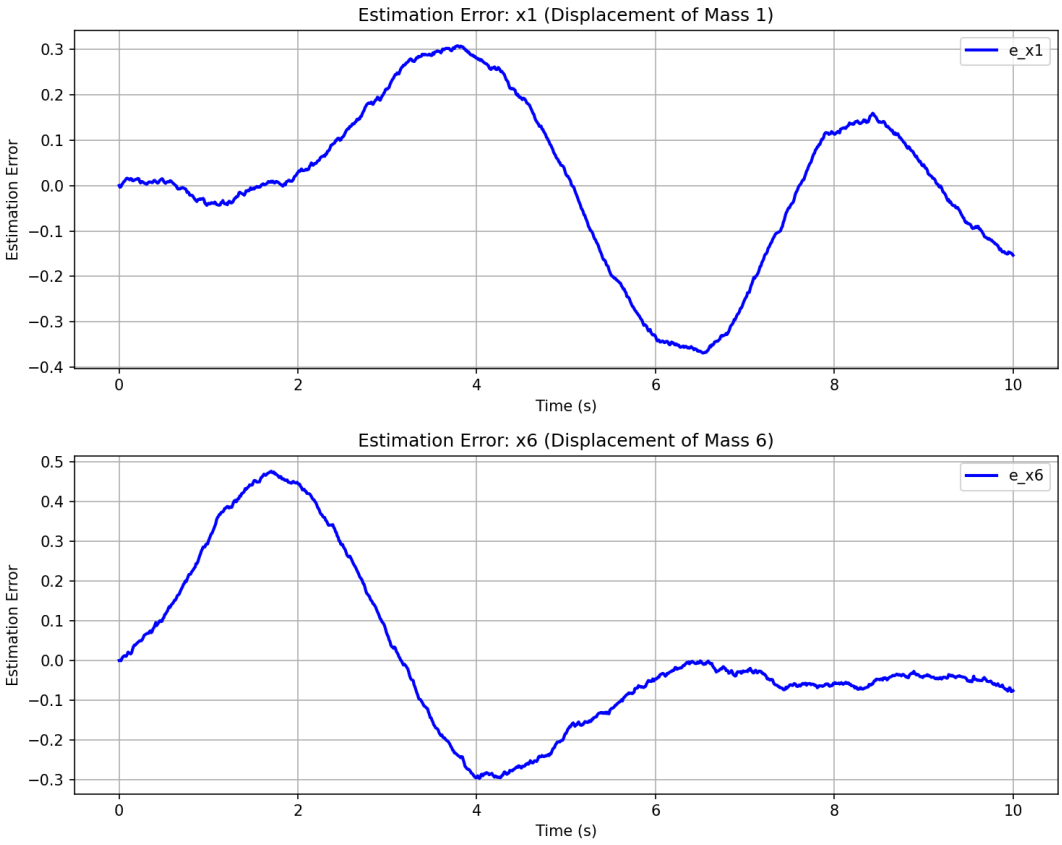

Figure 18: Estimation errors for the measured displacement states. Both e_{x_1} and e_{x_6} remain bounded and improve after the transient, consistent with steady-state filtering behavior.

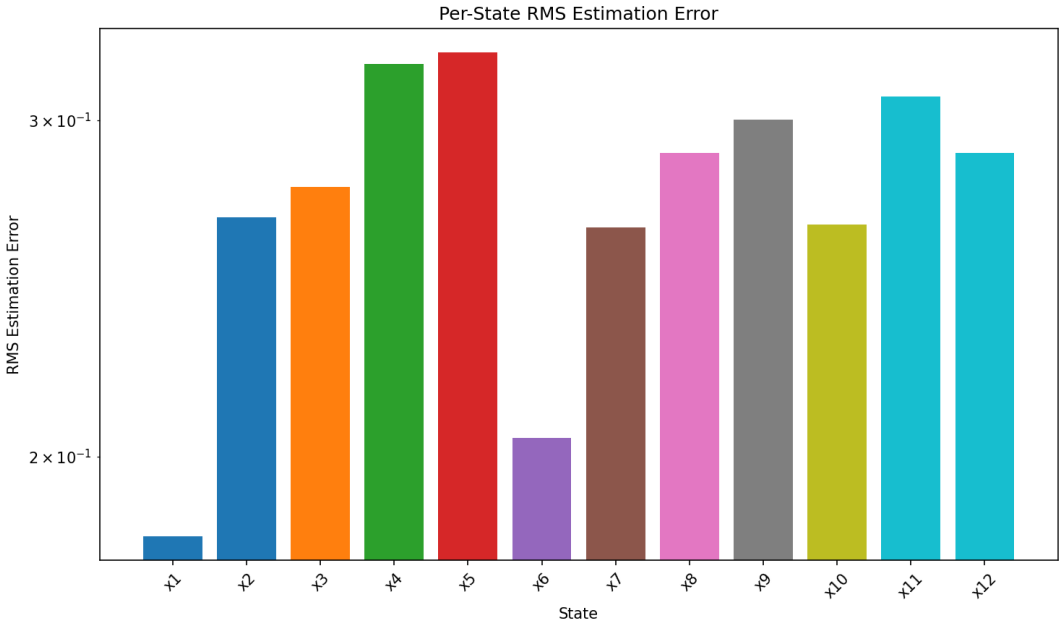

Figure 19: Per-state RMS estimation error across all 12 states. The directly measured states (x_1 and x_6) exhibit lower RMS error than several unmeasured states, while all states remain estimable with bounded error.

7.6 Comparison with Part 2 Observer

Feature	Part 2 Observer	Part 5 Kalman Filter
Design method	Pole placement	DARE (optimal)
Noise handling	None	Process + measurement
Optimality	Suboptimal	Optimal (minimum error covariance)

Table 6: Comparison of deterministic observer and stochastic Kalman filter.

7.7 Findings

- The Kalman filter explicitly incorporates both process noise and sensor noise through (Q_w, R_v), producing an estimator tuned for uncertainty rather than deterministic convergence.
- The steady-state RMS error is approximately 45% lower than the full-window RMS error, showing that the filter converges from an initial transient to a lower steady-state error level.
- The estimator spectral radius $\rho(A_d - L_k C) = 0.999547$ is strictly below unity (stable) but close to one, which is consistent with an optimal trade-off between responsiveness (tracking) and noise rejection for a lightly damped system.
- Using only two noisy displacement measurements (x_1 and x_6), the filter produces bounded estimates of all 12 states, enabling LQG synthesis in Part 6 by combining this estimator with the LQR controller.

8 Part 6: LQG Controller

8.1 Objective

In this part, we combine the optimal state-feedback controller from Part 3 (discrete-time LQR) with the optimal state estimator from Part 5 (steady-state Kalman filter) to obtain an LQG (Linear Quadratic Gaussian) controller for the noisy 6-mass spring system. The resulting controller computes the control input using the estimated state $\hat{x}[k]$ reconstructed from noisy measurements, enabling near-optimal regulation when the true state is not directly available.

8.2 LQG structure

The LQG controller combines the LQR gain K from Part 3 with the Kalman filter gain L_k from Part 5. By the separation principle, these gains are designed independently and then connected: $u[k] = -K\hat{x}[k]$, where $\hat{x}[k]$ is produced by the Kalman filter. The stochastic system model and noise covariances (Q_w, R_v) follow Part 5.

8.3 Closed-loop dynamics

The LQG loop consists of:

$$\hat{x}[k+1] = A_d\hat{x}[k] + B_d u[k] + L_k\big(y_{\text{meas}}[k] - C\hat{x}[k]\big), \tag{53}$$

$$u[k] = -K\hat{x}[k]. \tag{54}$$

The controller uses only the estimate $\hat{x}[k]$ reconstructed from noisy measurements.

8.4 Cost function under measurement noise

The quadratic performance index is evaluated using the *true* output

$$y_{\text{true}}[k] = Cx[k], \tag{55}$$

rather than the noisy measurement $y_{\text{meas}}[k]$. This avoids artificially inflating the cost by penalizing uncontrollable sensor noise:

$$J = \sum_{k=0}^{N-1}\Big(u[k]^\top u[k] + y_{\text{true},1}[k]^2 + y_{\text{true},6}[k]^2\Big). \tag{56}$$

8.5 Results

The LQG controller reuses the gains from previous parts:

- $K \in \mathbb{R}^{3\times 12}$ (from Part 3, unchanged).
- $L_k \in \mathbb{R}^{12\times 2}$ (from Part 5, unchanged).

Numerical results for the noisy closed-loop simulation are:

- Total cost: $J = 4.260967 \times 10^2$.
- Maximum input magnitude: $\max_k \|u[k]\|_\infty = 4.086037 \times 10^{-1}$.
- RMS estimation error: $\text{RMS}\big(\|x - \hat{x}\|\big) = 9.573350 \times 10^{-1}$.
- RMS estimation error (last 20% of samples): 5.593296×10^{-1}.

Metric	Part 3 (No Noise)	Part 6 (LQG with Noise)
Total cost J	9.057×10^7	4.261×10^2
Max $\|u\|_\infty$	3.597×10^3	4.086×10^{-1}
Estimator	Pole placement (L)	Kalman filter (L_k)
Controller	LQR (K)	LQR (K), same gain

Table 7: Comparison of Part 3 (deterministic) and Part 6 (stochastic LQG).

8.6 Figures

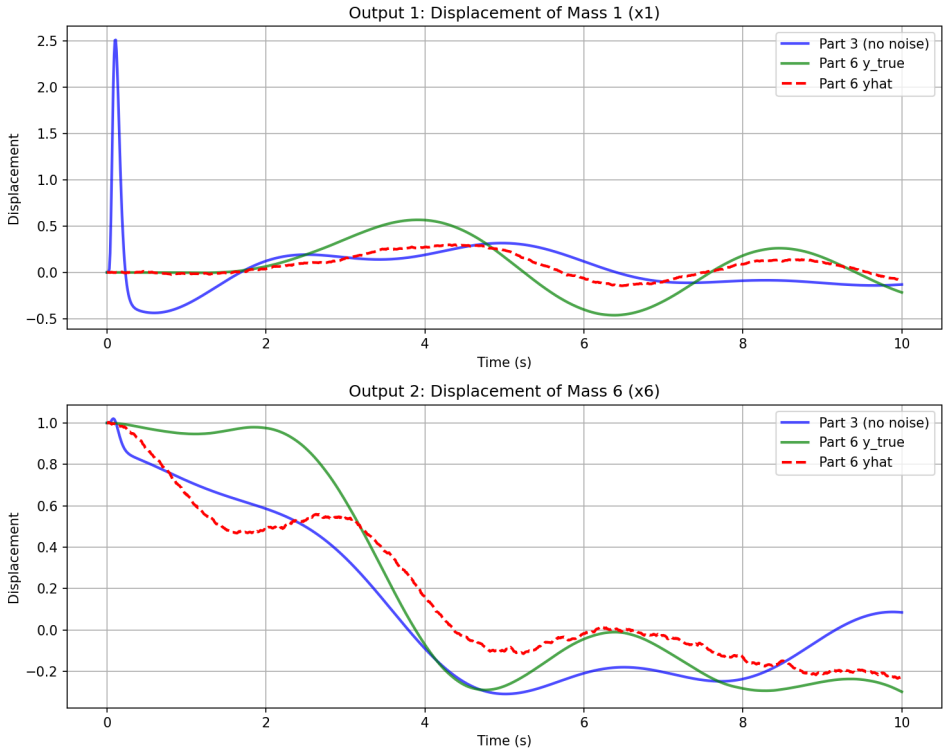

Figure 20: Outputs comparison between Part 3 baseline (no noise) and Part 6 LQG (noisy). The LQG outputs remain regulated despite process and measurement noise.

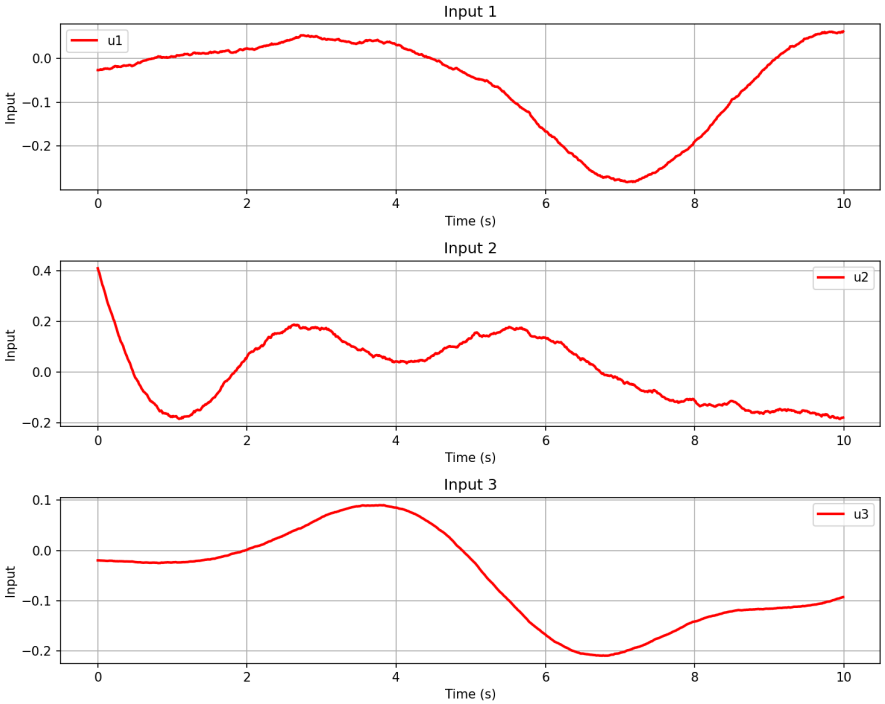

Figure 21: LQG control inputs u_1, u_2, u_3 generated by $u[k] = -K\hat{x}[k]$. The inputs remain bounded and are substantially smaller in magnitude than the deterministic Part 3 case.

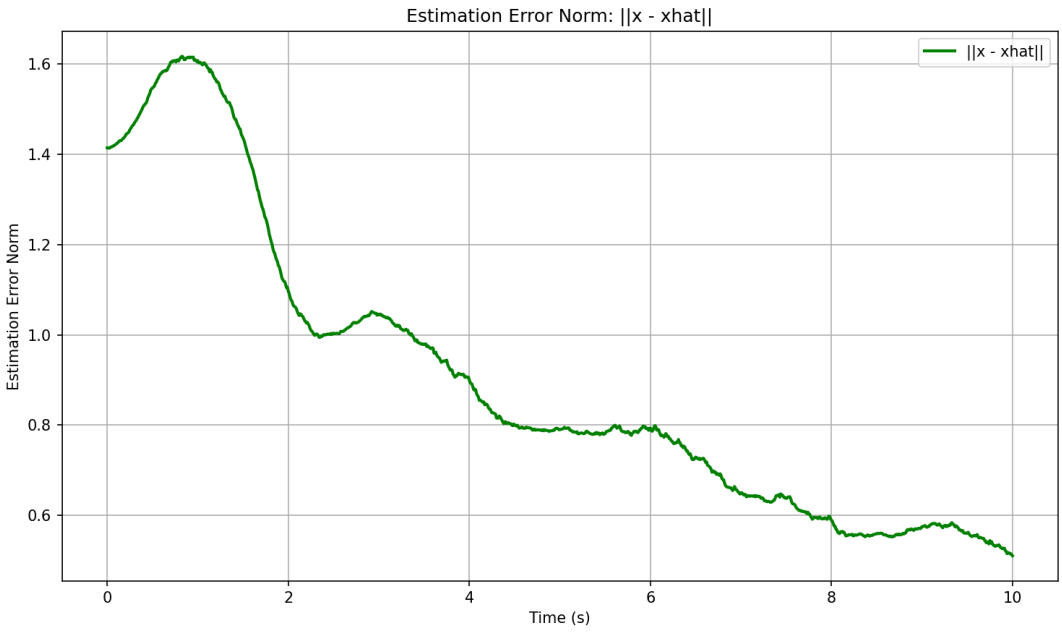

Figure 22: Estimation error norm $\|x[k] - \hat{x}[k]\|$ under process noise and measurement noise. The Kalman filter maintains bounded estimation error suitable for feedback control.

8.7 Findings

- **Separation principle in practice.** The LQG controller is formed by combining the independently designed K (LQR) and L_k (Kalman filter), without re-tuning either gain.
- **Stabilization under uncertainty.** Despite process and measurement noise, the outputs remain regulated, and the estimator provides usable state estimates from two noisy measurements.
- **Control effort reduction.** The maximum input magnitude decreases from 3.597×10^3 (Part 3) to 4.086×10^{-1} (Part 6), which is approximately a four-order-of-magnitude reduction.
- **Estimator convergence behavior.** The RMS estimation error over the last 20% of the horizon is lower than the full-window RMS, indicating convergence toward a steadier filtering regime during closed-loop operation.

9 Part 7: Sensor Augmentation Analysis

9.1 Objective

This part investigates how adding additional position sensors affects (i) state-estimation quality and (ii) closed-loop regulation performance under the same LQG control framework as Part 6. The baseline is the Part 6 LQG setup with two measured outputs. Two augmented sensing configurations are evaluated to quantify how much additional measurement information improves estimation and, through improved feedback, reduces the regulation cost.

9.2 Sensor configurations

Three sensing configurations are compared, all estimating the same 12-state vector but differing in the measurement matrix $C_{\text{meas}} \in \mathbb{R}^{p\times 12}$:

- **Baseline (2 sensors):** measures (x_1, x_6), i.e., $p = 2$.
- **Case 1 (4 sensors):** measures (x_1, x_2, x_5, x_6), i.e., $p = 4$.
- **Case 2 (6 sensors):** measures all positions $(x_1, \ldots, x_6)$, i.e., $p = 6$.

9.3 Design principles

- **Controller unchanged:** The LQR gain K from Part 3 is fixed for all configurations; $u[k] = -K\hat{x}[k]$.
- **Estimator redesigned:** The Kalman filter gain L_k is recomputed for each C_{meas} via the DARE.
- **Cost fixed:** The regulation cost (8) penalizes (x_1, x_6) regardless of sensor count.
- **Noise:** $Q_w = 0.05\, I_3$, $R_v = 0.1\, I_p$ (dimension changes with p).

9.4 Results

Table 8 summarizes regulation performance and estimator behavior across sensor configurations. The steady-state RMS error refers to the RMS of $\|x - \hat{x}\|$ over the steady-state portion of the simulation (last 20% of samples, consistent with Part 6).

Config	Sensors	Cost J	RMS Error (SS)	Spectral Radius
Part 6	2 (x_1, x_6)	426.1	0.559	0.999547
Case 1	4 (x_1, x_2, x_5, x_6)	401.8	0.464	0.998968
Case 2	6 $(x_1$–$x_6)$	371.0	0.270	0.998415

Table 8: Sensor augmentation analysis results.

In all cases, the controller gain K is identical, so the peak input magnitude is unchanged across configurations (the simulations report the same $\max_k \|u[k]\|_\infty$), and the main effect of additional sensors is improved estimation quality through a redesigned L_k.

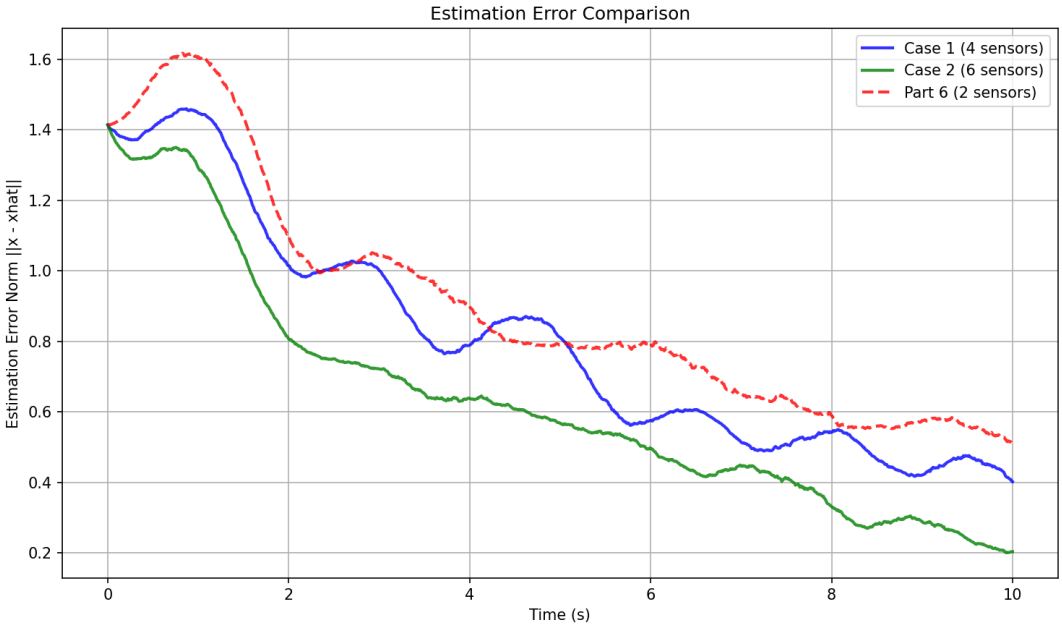

Figure 23: Estimation error norm comparison $\|x - \hat{x}\|$ for baseline (2 sensors) and augmented sensing (4 and 6 sensors).

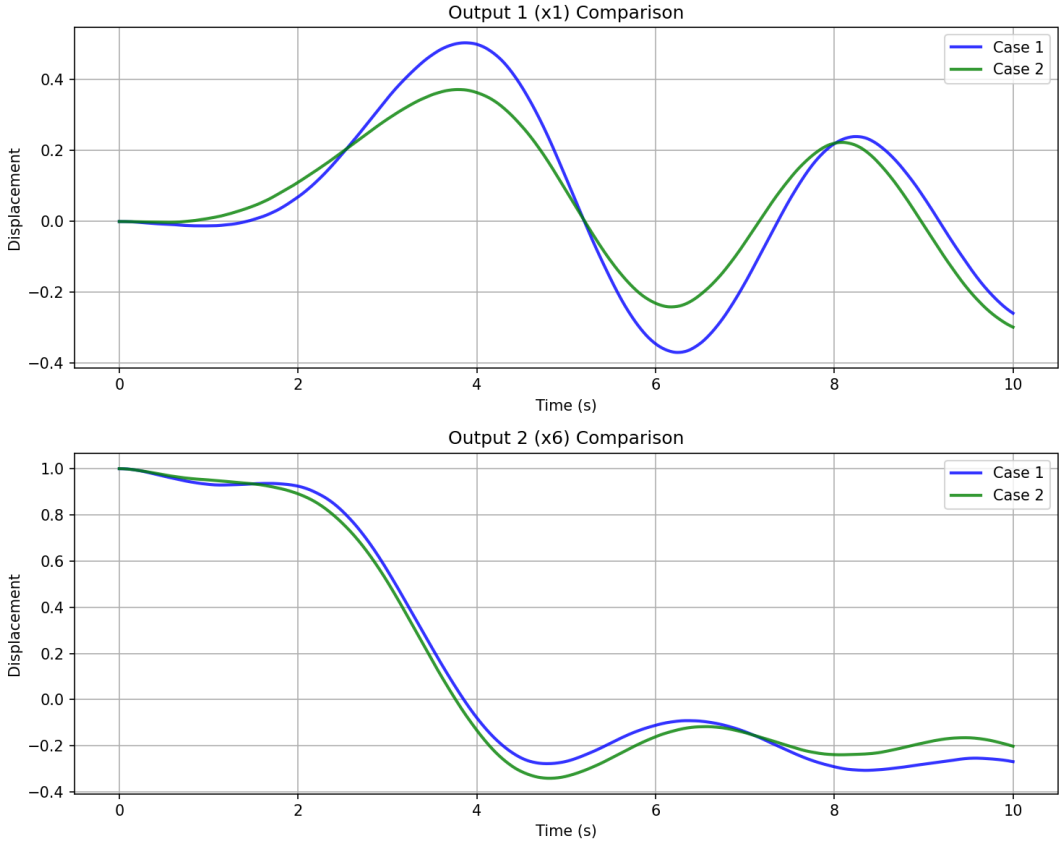

Figure 24: Output comparison for $y_1 = x_1$ and $y_6 = x_6$ under augmented sensing. Improved estimation yields improved regulation of the same cost outputs.

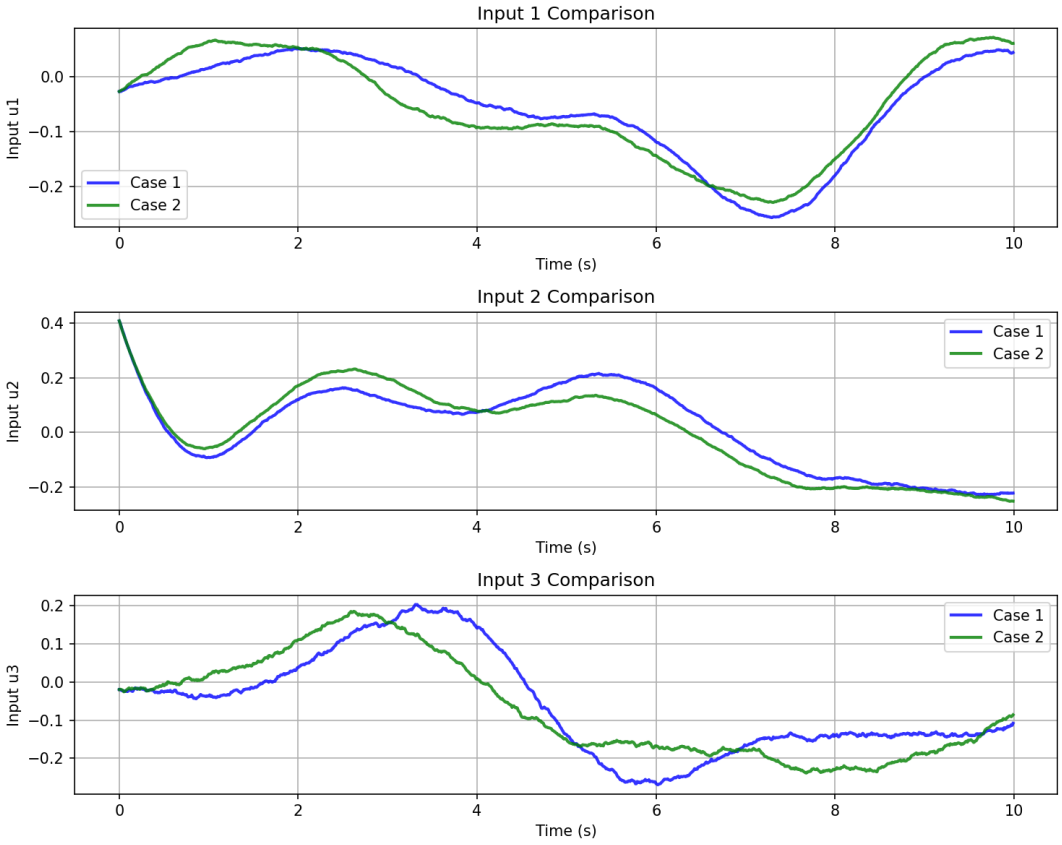

Figure 25: Input comparison for u_1, u_2, u_3 under augmented sensing. Because K is unchanged, the control effort scale remains comparable across configurations.

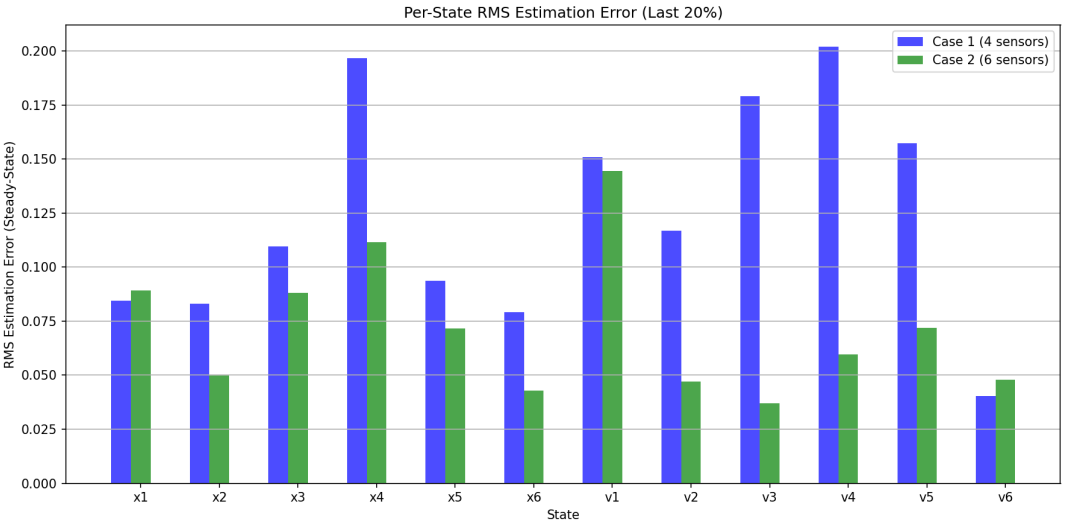

Figure 26: Per-state steady-state RMS estimation error comparison under augmented sensing. Adding sensors reduces estimation error for unmeasured states via improved observability through measurement fusion.

9.5 Performance improvements and diminishing returns

Using the baseline (2-sensor) steady-state RMS error 0.559 and cost 426.1, the relative improvements are:

- **2 to 4 sensors:** steady-state RMS error improves by 17.0% (from 0.559 to 0.464), and cost decreases by 5.7% (from 426.1 to 401.8).
- **2 to 6 sensors:** steady-state RMS error improves by 51.7% (from 0.559 to 0.270), and cost decreases by 12.9% (from 426.1 to 371.0).

The results show that added sensing can produce large estimation gains, especially when moving toward full position sensing. Regulation gains, measured through the fixed cost in (8), increase more moderately because the cost penalizes only (x_1, x_6). This highlights a practical saturation effect: beyond a point, improved global state estimation does not translate one-to-one into reduced cost when the objective depends on only a subset of outputs.

9.6 Findings

- **More sensors improve estimation and regulation.** Both steady-state RMS estimation error and total cost decrease as sensors are added.
- **Estimator convergence improves.** The estimator spectral radius decreases from 0.999547 to 0.998968 and 0.998415, indicating faster estimator dynamics with richer measurements.
- **Estimation improvement exceeds regulation improvement.** Estimation error decreases strongly with more sensors, while the cost reduction is moderated by the fixed cost structure that penalizes only (x_1, x_6).
- **Control effort scale is unchanged.** Since K is unchanged, input magnitudes do not increase with added sensors. The main benefit comes from providing a more accurate feedback signal $\hat{x}$ for the same controller.
- **Practical trade-off.** Additional sensors increase instrumentation cost and complexity. The table quantifies the performance gains available from 4 and 6 sensors, enabling a cost-benefit decision based on application constraints.

10 Conclusion

10.1 Summary of key findings

Parts 0–1 (System analysis). The discrete-time model was validated through open-loop simulation. Observability analysis showed that a single position sensor provides only partial observability (rank 6/12). Adding a second sensor at x_6 achieves full observability (rank 12/12), enabling complete state reconstruction.

Parts 2–4 (Deterministic control). A Luenberger observer estimated all 12 states from two measurements (x_1, x_6). Using these estimates, the LQR controller stabilized the plant, demonstrating the separation principle. Reduced actuation (removing u_3) increased the total cost by approximately 49%, illustrating the trade-off between actuator availability and achievable performance.

Parts 5–7 (Stochastic control). A steady-state Kalman filter provided optimal state estimation under process and measurement noise. The LQG controller (LQR + Kalman) successfully regulated the noisy system. Sensor augmentation showed that steady-state estimation error improved by up to 51.7% and cost decreased by up to 12.9% when moving from 2 to 6 sensors, with diminishing returns.

10.2 Key learnings

- **Observability is critical for state estimation.** Without sufficient measurement information, full-state reconstruction is impossible regardless of estimator design.
- **Separation principle supports modular design.** The estimator and controller can be designed independently and then combined in closed loop using estimated states.
- **Kalman filtering is preferable under noise.** For stochastic systems, the Kalman filter provides an optimal estimator and typically outperforms pole-placement observers when process and measurement noise are present.
- **Actuator availability strongly affects performance.** Fewer inputs reduce achievable performance and can increase the required effort from remaining actuators.
- **Additional sensors improve estimation with diminishing returns.** More measurements reduce estimation uncertainty and can improve regulation, but marginal gains decrease as the sensor set becomes increasingly informative.

10.3 Design recommendations

- **Minimum sensing for full estimation:** Use at least two sensors at (x_1, x_6) to ensure full observability and enable complete state estimation.
- **Sensor augmentation trade-off:** A 4 to 6 sensor configuration yields the best performance-to-instrumentation trade-off in this study, improving estimation and reducing regulation cost beyond the 2-sensor baseline.

- **Actuation:** Prefer full actuation (3 inputs) when possible. Reduced actuation remains viable but incurs a substantial performance penalty (about 49% cost increase in the tested setting).
- **Estimator choice in practice:** Use a Kalman filter for noisy environments, since it explicitly incorporates noise statistics and yields an optimal steady-state gain.

Final remarks. Across Parts 0 through 7, a complete control-design pipeline was demonstrated for a high-order, lightly damped mechanical system. The workflow progressed from model verification and structural analysis (observability) to deterministic estimation and optimal control (observer/LQR), and then to stochastic estimation and control (Kalman filter/LQG), concluding with a systematic assessment of sensing augmentation.

The results demonstrate how sensing and actuation constraints shape achievable closed-loop performance. They also show that optimal estimation and control tools provide a principled framework for robust regulation under uncertainty.